Multistage phase transitions in photoexcited ReS_2 monolayer: Real-time time-dependent density functional theory calculations

Liyuan Chen (陈丽媛),[1] Li Chen (陈立),[1] Hongli Chen (陈红丽),[1] Liyan Shang (商丽燕),[1] Yawei Li (李亚巍),[1] Liangqing Zhu (朱亮清),[1] Shijing Gong (龚士静),[1] and Zhigao Hu (胡志高)[1,2,*]

[1]*Technical Center for Multifunctional Magneto-Optical Spectroscopy (Shanghai), Engineering Research Center of Nanophotonics and Advanced Instrument (Ministry of Education), Department of Physics, School of Physics and Electronic Science, East China Normal University, Shanghai 200241, China*

[2]*Collaborative Innovation Center of Extreme Optics, Shanxi University, Taiyuan, Shanxi 030006, China*

(Received 23 May 2024; revised 22 December 2024; accepted 15 January 2025; published 23 January 2025)

Photoinduced phase transitions (PIPTs) allow complex interactions to be distinguished within the constraints of atomic motion. Here, using real-time time-dependent density functional theory (rt-TDDFT) simulations combined with occupation-constrained density functional theory (DFT) methods, we reveal the ultrafast dynamics of ReS_2 monolayer driven by photoexcitation at varying levels of electronic occupancy. The results show that the phase transition from diamond-shaped to zigzag-shaped to quasi-diamond-shaped (DS-ZS-DS′) is effectively induced by 4% excitation manually, resulting in the formation of new quasidiamond chains along the direction of the original diamond chains rotated by $\pi/3$. Notably, under pulse excitation, the entire dynamic process also includes subsequent recovery, during which the quasidiamond chains rotate back to their original direction. The phase transition is mediated by the atomic force caused by photoexcited electrons occupying the antibonding state of the Re-Re bonds between the Re_4 diamonds, accompanied by the modulation of the potential energy surface. The thermal phonon vibration can effectively reduce the optical excitation fluency required to drive the bond dissociation and rearrangement. These findings provide an important guiding significance for nonequilibrium phase regulation.

DOI: 10.1103/PhysRevB.111.024111

I. INTRODUCTION

Phase engineering of two-dimension transition-metal dichalcogenides (2D TMDs) via regulating the atomic structure provides a huge platform for manipulating their diverse physical and chemical properties [1–3]. Rhenium disulfide (ReS_2) with diamond-shaped (DS) phase has attracted considerable interest due to its layer-independent electrical and optical properties [4,5]. Due to the unique DS chain structure, the fundamental physical properties of ReS_2 are anisotropic in plane [6,7]. So far, it has been successfully synthesized and stripped experimentally by a variety of methods [8–10]. In recent years, the topic of effectively regulating the electronic properties of ReS_2 by changing the atomic arrangement has been a topic of attention [11–13]. At elevated temperatures, the atomic orientation of DS chains can be regulated by electron beam irradiation, which is directly related to the electron transport anisotropy in ReS_2 monolayer [14]. The vacancy and strain caused by electrochemical treatment and high density electron doping through Li treatment lead to the formation of grain boundarie of DS chains with different orientations [15,16]. Despite extensive studies, intense optical or electrical pulses inevitably lead to the presence of thermal effects, accompanied by a loss of performance. In addition, the calculations based on the total energy of the ground state have certain limitations in resolving the phase transition path of nonequilibrium processes.

Ultrashort pulsed lasers can effectively suppress thermal effect and have great potential in atomic-level phase modes. By regulating electronic excitation, bond dissociation and atomic rearrangement are achieved to obtain the desired electronic and optical properties on ultrafine timescales. Photoinduced phase transitions (PIPTs) of ultrafine laser pulses arise from the interplay among charges, orbits, and lattice degrees of freedom in the material. Theoretical modeling allows the identification of complex interactions between different degrees of freedom under the constraints of atomic motion, which provides an ideal platform to fill in the shortcomings in experiments. In addition, the identification of thermal phonon contributions during PIPTs has become the focus of understanding ultrafast phase transition processes [17,18].

In this work, we investigate PIPTs in ReS_2 monolayer using real-time time-dependent density functional theory (rt-TDDFT) simulations combined with occupation-constrained DFT calculations [19–21]. Two different methods were applied to rt-TDDFT simulations to elucidate the microscopic driving forces that promote the structural phase transition of ReS_2. First, photoexcitation is achieved by promoting valence electrons from the top of the valence bands to the bottom of the conduction bands. The precise control of electronic excitation through the manual definition of initial conditions is an effective approach in both early and recent rt-TDDFT research [22–25]. The excitation intensity is expressed as the

*Contact author: zghu@ee.ecnu.edu.cn

percentage of the number of excited electrons n in the total number of valence electrons. The excitation of 4% valence electrons effectively induces the phase transition from diamond-shaped to zigzag-shaped to quasi-diamond-shaped (DS-ZS-DS′) phase of ReS_2 monolayer. With the breaking of the Re_4 diamonds and the formation of new bonds between parallel DS chains, the new quasidiamond chains are formed with their direction rotated by $\pi/3$ relative to the original diamond chains. The microscopic driving force for the separation of the Re_4 clusters is provided by the occupation of the antibonding states of the Re-Re bonds. However, the photoexcited electrons extend into higher energy regions over time, which hinders further phase transitions from the DS′ configuration. Secondly, an external electric field is used to represent a laser pulse with a Gaussian shape during rt-TDDFT simulation: $E(t) = E_0 \cos(\omega t) \exp[-(t - t_0)^2/(2\sigma^2)]$, where E_0 = 0.1 V/Å, the pulse width 2σ = 25 fs and the photon energy $\hbar\omega$ = 2.47 eV, which represents the 500-nm optical pump pulse. Over time, the number of excited electrons is between 4.3% and 4.9%. The laser pulse can achieve a further phase transition of the DS′ phase, which is due to the fact that there is always a part of the excited electrons localized to the bottom of the conduction band over time, providing the microscopic force that drives the diamond chain to break again. In addition, we also demonstrate bond dissociation and rearrangement driven by atomic forces caused by the cooperation of photoexcitation and thermal phonon vibrations at room temperature.

II. RESULTS AND DISCUSSION

ReS_2 with $P\bar{1}$ (No.2) space group has trilinear symmetry in the crystal structure, as shown in Fig. 1(d). The presence of an additional d electron causes ReS_2 to stabilize in a Peierls distortion with the adjacent Re atoms form Re_4 diamond chains along the b[010] axis, as confirmed by high-resolution transmission electron microscopy [26] and DFT simulations [5]. The PIPTs process in momentum space can be further explored by evaluating the influence of photoinduced electrons on chemical bonds. The crystal orbit Hamilton population (COHP) curves in Fig. 1(a) show that the Re-Re bonds and Re-S bonds both present antibond distribution above the Fermi level (for details of calculation methods see Sec. IV). The Re-S bonds are still in the antibonding states near the top of the valence bands. The Re-Re bonds exhibit an extremely small antibond distribution at the top of the valence bands, while the bonding distribution ranges from −0.45 eV to −3.37 eV. The high excitation moves most of the electrons in the Re-Re bonding bands to the antibonding bands above the Fermi level, which is a possible source of instability in the crystal structure. The projected band structure of the d-orbit is shown in Fig. 1(b). The electronic states near the top of the valence bands and the bottom of the conduction bands are mainly dominated by the $d_{x^2\text{-}y^2}$ and d_{xy} orbitals [27]. The strong interaction between d_{xy} and $d_{x^2\text{-}y^2}$ orbital electrons in the plane plays a significant role in lattice distortion [28]. As the energy moves away from the top of the valence band and the bottom of the conduction band, the dominant contribution of the d_{z^2}, d_{xz}, and d_{yz} orbits appears in turn.

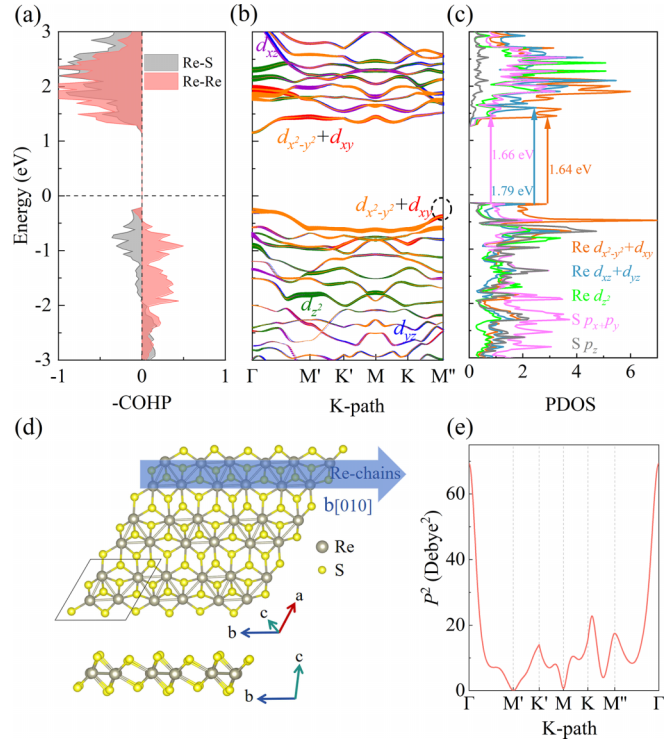

FIG. 1. (a) Crystal orbital Hamilton population (COHP) bonding analysis of Re-Re bonds and Re-S bonds, respectively. (b) Band structure along high-symmetry points for ReS_2 monolayer, the weights of the Re-d oribits are color-coded. (c) The decomposed projected density of states (PDOS) for the p orbitals of S atoms and the d orbitals of Re atoms. The arrows represent optical transitions with different electronic excitation energies. (d) Top and side views of the diamond-shaped (DS) phase structure from the ReS_2 monolayer. (e) Transition matrix elements between the highest valence band and lowest conduction band along high-symmetry points.

Carrier excitation is closely related to peaks in DOS and transition dipole moments between bands [29,30]. The dominant peaks in ReS_2 are represented by arrows in Fig. 1(c), where the optical transitions correspond to excitation energies of 1.64, 1.66, and 1.79 eV. By calculating the squares of the dipole transition matrix elements, P^2, the transition probability between the highest valence band and the lowest conduction band can be further revealed. Specifically, there are large dipole transition matrix elements between highest point of the valence band and the lowest point of the conduction band near the Γ point [Fig. 1(e)]. Therefore, optical excitation is predicted to occur when the laser energy exceeds 1.64 eV (corresponding to 756 nm).

Prior to rt-TDDFT calculations, we first performed *ab initio* molecular dynamics (AIMD) simulations to examine the effect of photoexcitation on the structural phase transition of ReS_2 monolayer (Sec. V). The snapshot of the structure over time shows that structural deformation and Re_4 cluster dissociation do not occur at room temperature. The total energy curve indicates that ReS_2 monolayer is thermally stable. In contrast, in rt-TDDFT calculations of manually excited electrons, the complete structural phase transition can be induced by reaching 4% excitation [Figs. 2(a)–2(c)]. Due to the electronic excitation, the Re_4 rhomboid chains break and

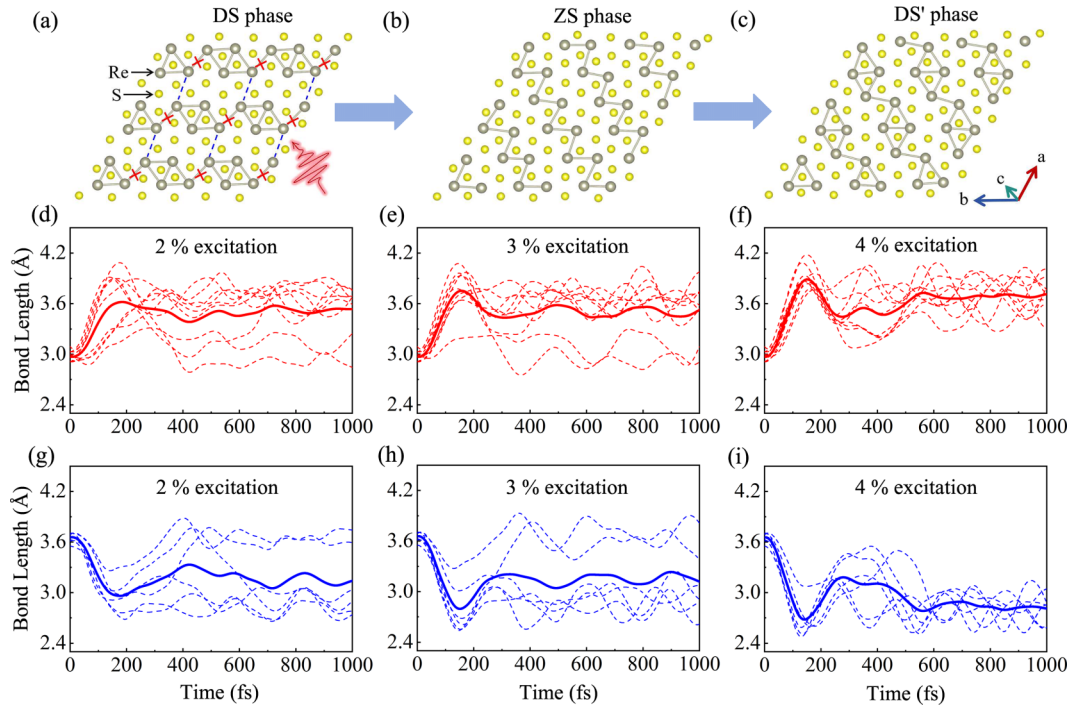

FIG. 2. [(a)–(c)] Photoinduced ultrafast phase transition for ReS_2 monolayer with 4% of electrons transferred to the conduction bands at the initial time. The atomic structures for ReS_2 monolayer in diamond-shaped (DS) phase, zigzag-shape (ZS) phase and quasi-diamond-shaped (DS′) phase, respectively. [(d)–(i)] Bond length evolution under different electronic excitations. The red and blue dashed lines represent the evolution of the nine Re-Re bond lengths ($d_{\text{Re-Re}}$) and six non-Re-Re bond lengths ($d'_{\text{Re-Re}}$), respectively, as shown by the red crosses and blue dashed lines in the upper part. The solid line represents the average bond length.

new quasirhombic chains are formed in the rotation direction of $\pi/3$, resulting in the transformation of DS towards DS′ phase. The dissociation of the Re_4 diamond chains and the bonding between parallel chains are the direct descriptors of the phase transition. The lengths between the two types of Re-Re pairs are defined as $d_{\text{Re-Re}}$ and $d'_{\text{Re-Re}}$. By exciting different numbers of valence electrons, the evolution of $d_{\text{Re-Re}}$ and $d'_{\text{Re-Re}}$ bond lengths can be tracked over time [Figs. 2(d)–2(i)]. The 2% and 3% electronic excitation cause the partial $d_{\text{Re-Re}}$ bond lengths to increase rapidly beyond the threshold distance for Re-Re bonding (3.2 Å) [31], demonstrating the breaking of the partial Re_4 diamond chains. At the same time, the distance between some $d'_{\text{Re-Re}}$ pairs decreases until they reach below 3.2 Å to form chemical bonds. Structural snapshot of 4% excitation shows extensive bond breaking of $d_{\text{Re-Re}}$ pairs and the recombination of the $d'_{\text{Re-Re}}$ pairs within 1 ps. The bond lengths of the two sets of Re-Re pairs show large random fluctuations, so the photoexcited dynamic process is more inclined to disordered motion. The DS′ structure cannot be straightforwardly described as the result of $\pi/3$ rotation of the entire DS structure due to the nonuniform oscillating behavior of the bond lengths, so the DS′ structure is classified as the quasidiamond phase. Remarkably, the breaking and recombination of the Re-Re bonds first induce the formation of transient Re-Re zigzag chains around 80 fs, aligned with the direction of the original DS chains rotated by $\pi/3$. The emergence of transient structures has been reported in studies investigating various photoexcited phase transitions, such as in GeTe and $MoTe_2$ [32,33]. Subsequently, because of the combined effect of the atomic driving force caused by photoexcited electrons and the thermal phonon vibrations, the Re atoms rearrange along the zigzag direction for a period of time before starting to form the large-scale quasidiamond chains, corresponding to the DS′ phase, at approximately 700 fs. The evolution of the distance between adjacent Re-Re atoms in the zigzag direction further confirms the transition from zigzag to quasidiamond shape (Sec. VI, Fig. 7).

Identifying the relation between atomic driving force and atomic motion is an effective way to describe PIPTs. The real-space charge distribution of photoexcited electrons and holes on the (001) plane at different excitations in the initial state is shown in Figs. 3(a) and 3(b). The distribution of photoexcited carriers in the d_{xy} and $d_{x^2-y^2}$ orbitals results in the changes in bond lengths and bond angles in the x-y plane. The photoexcited electrons are mainly distributed around the Re atoms connected to the Re_4 diamonds at 2% excitation, which mainly reflects the characteristics of the antibonding orbitals of the Re-Re bonds. When electrons are excited from the bonding state to the antibonding state, the total energy of the system correspondingly increases [17,20]. To reduce the energy of the excitation system, a corresponding tensile driving force is generated between the adjacent Re_4 units to induce an increase in the Re-Re bond length. When the number of photoexcited electrons increases from 2% to 4%, the photoexcited electron density not only increases significantly in the distribution of Re atoms connected to adjacent Re_4 units, but also begins to appear around other Re atoms in Re_4 units. Therefore, the change in bond length and bond angle is also influenced by the other Re atoms, which is reflected in the driving force on the Re atoms [Fig. 3(c)].

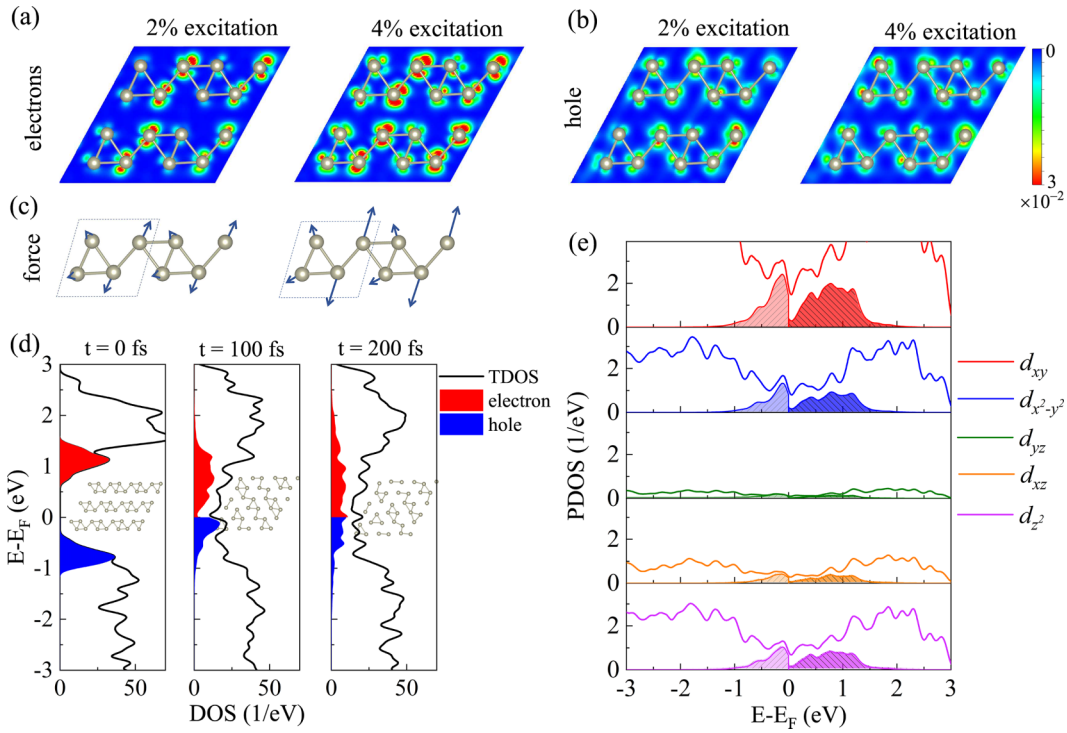

FIG. 3. Real-space distribution of the excited (a) electrons and (b) holes under 2% and 4% excitations on the (001) plane in the initial state. (c) The atomic driving force caused by photoexcitation on the (001) plane in the case of 2% and 4% excitations. The magnitude and direction of the arrows are defined as the magnitude and direction of the driving forces. (d) Evolution of density of states (DOS) of photoexcited electrons and holes under 4% excitation. The illustrations represent structural snapshots at different times. (e) The d-orbital decomposed partial density of states (PDOS) of Re atoms under 4% excitation at 100 fs, where the distribution of photoexcited electrons and holes in different orbitals is encoded by color shadows.

By tracking the density of states (DOS) under photoexcitation, it is found that the occupancy of photoexcited electrons and holes has a certain regularity. In the initial state, electrons are excited to the bottom of the conduction bands. Over time, photoexcited electrons and holes are distributed over a wider energy region of conduction bands and valence bands, accompanied by semiconductor-to-metal transition [Fig. 3(d)]. The reduction of the electrons occupying the antibonding orbitals at the bottom of the conduction band results in a tension driving force that is much smaller than the force driving the DS′ phase transition. Once valence electrons are excited beyond a certain threshold above the conduction band minimum, nonthermodynamic processes are unlikely to occur within a short timescale [34]. In theory, further driving the DS′ phase transition may require more electron excitation or a sufficiently long time. In addition, to specify the hopping path of photoexcited electrons, we explored the Re-d orbital-decomposed PDOS [Fig. 3(e)]. It is evident that the $d_{x^2\text{-}y^2}$ and d_{xy} orbitals have the highest priority occupation when a large number of electrons in the bonding state are excited to the antibonding state, followed by d_{z^2}, which corresponds to Fig. 1(b).

Considering that manually excited electrons and external electric fields simulating laser pulses may lead to different dynamic processes, we further carried out the rt-TDDFT calculation under pulse excitation. The results demonstrate that a 500 nm optical pump pulse with a duration of 120 fs contains a reversible process in which the rhombic chain in the DS′ phase returns to its original direction (Fig. 4). Due to the inability of pulse excitation to control the excited electrons precisely, the statistical proportion of excited electrons that transition

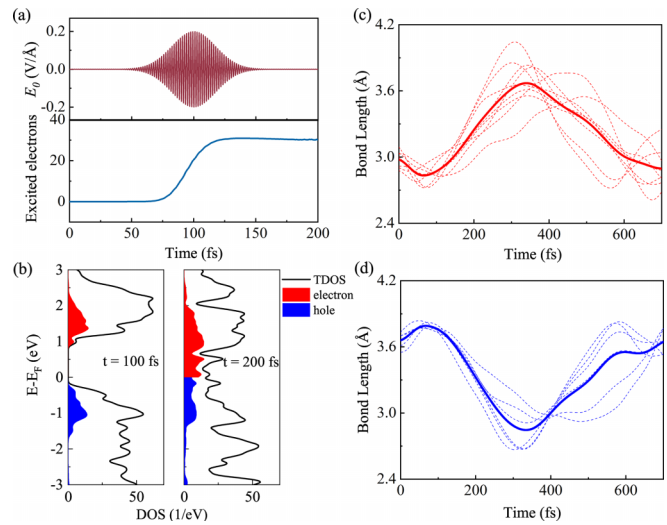

FIG. 4. (a) The shape of the external electric field applied to ReS_2 with laser strength $E_0 = 0.1$ V/Å, and the number of photoexcited electrons as a function of time. (b) Evolution of DOS of photoexcited electrons and holes under pulse excitation. The (c) red and (d) blue dashed lines represent the evolution of the $d_{\text{Re-Re}}$ bonds and $d'_{\text{Re-Re}}$ bonds, respectively. The solid line represents the average bond length.

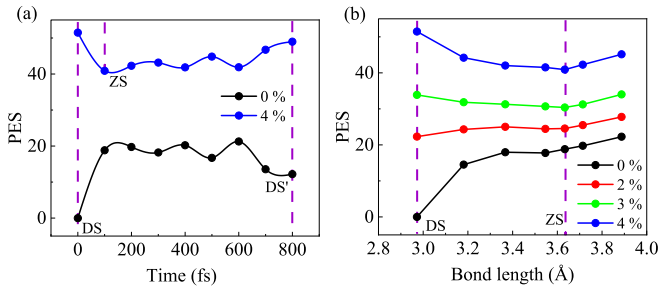

FIG. 5. (a) The evolution of the potential energy surfaces (PESs) from DS phase to DS′ phase with time. (b) The PESs from DS phase to ZS phase as a function of the averaged length of $d_{\text{Re-Re}}$ pairs.

from valence bands to conduction bands is between 4.3% and 4.9% of the total valence electrons. Pulse excitation makes the distance of $d_{\text{Re-Re}}$ pairs increase first and then decrease in the range of 600 fs, while the opposite is true for $d'_{\text{Re-Re}}$ pairs. In simpler terms, the laser pulse further drives the rhomboid chain of the DS′ phase to evolve towards the original direction. Figure 4(b) shows the occupations of photoexcited electron and hole under pulse excitation. Due to the energy limitation of pulsed excited electrons, there are still a large number of photoexcited electrons localized at the bottom of the conduction bands, resulting in the microscopic driving force that can still promote the further phase transition of DS′. However, since the light pulse is a gradual accumulation process, the rate at which it drives the breaking of the diamond chains is delayed compared to manually excited electrons.

Photoexcited electrons regulate the forces between the atoms and change the potential energy surface (PES), further manipulating the atomic motion. The PES calculated by the occupation-constrained DFT method for the case of constrained different numbers of electrons in antibonding states is shown in Fig. 5. The transition from DS phase to DS′ phase requires overcoming a large energy barrier in the ground state. With the filling of valence electrons in the conduction band, the barrier changes from convex to concave, which leads to rapid dissociation of the Re_4 diamond chains. At the lowest potential of the energy barrier, a metastable ZS phase appears. To further understand the effect of different photoexcitation on PES, the evolution from DS to ZS phase with the average length of the $d_{\text{Re-Re}}$ bonds is further amplified. With the increase of excited electrons, the upward-sloping PES first flattens out and then slopes downward, which makes it easier for atoms to leave the crystalline order. The potential energy difference between the DS phase and ZS phase is positively correlated with the number of excited valence electrons.

The driving force caused by orbital occupation can induce atoms to leave the original phase coherently. However, we observe the disordered behavior of the phase transition at different excitation fluency. To exclude the influence of thermal phonon vibration on the photoexcited phase transition, we perform the rt-TDDFT calculations in the initial state of 4% and 10% valence electrons occupying the conduction bands at T = 1 K (Sec. VII, Fig. 8). The driving force caused by 4% excitation is difficult to meet the criteria of coherent phase transition, so the length of nine Re-Re bonds and six non-Re-Re bonds does not change significantly within 1 ps. In the case of 10% excitation, it can be seen that the two types of bond lengths are coherently changed, with the breaking of nine Re-Re bonds and the bonding of six non-Re-Re bonds at 400 fs. The results show that the strong excitation of the initial state leads to the enhancement of coherent motion. It is proved that the presence of thermal phonon effectively reduces the excited state electrons required to drive the phase transition.

III. CONCLUSION

In summary, using rt-TDDFT simulations combined with occupation-constrained DFT calculations, we have observed the unique phase transition dynamics of the ReS_2 monolayer induced by photoexcitation. Under 4% manual excitation, the new quasidiamond chains can be formed by rotating $\pi/3$ along the direction of original Re_4 chains within 1 ps, accompanied by the breaking of the original diamond chains and bonding between adjacent parallel chains. Due to the variation in electronic occupancy, the 500-nm 120-fs laser pulse further facilitates the recovery from DS′ phase to the original phase. The photoexcited electrons regulate the interatomic forces, further reducing the potential barrier of phase transition from DS to ZS to DS′ phase, which is conducive to the dissociation and recombination of bonds. According to the real spatial distribution of photoexcited carriers, the photoexcited electrons mainly occupy the connecting bonds between the Re_4 diamonds. The occupation of the antibonding states in the Re-Re bonds creates an atomic driving force that decreases the system′s energy by elongating the bond length. Furthermore, we reveal that the phase transition of ReS_2 monolayer at room temperature is driven by the combination of electronic excitation and thermal phonon vibration. This work provides a unique perspective for understanding the PIPTs in ReS_2 monolayer and suggests an actionable avenue for ultrafast optical experiments.

IV. MATERIALS AND METHODS

The AIMD and rt-TDDFT simulations are performed in the *ab initio* package PWmat [35,36]. The calculations are carried out by norm-conserving pseudopotentials (NCPP) generated by the optimized norm-conservating Vanderbilt pseudopotentials (ONCVPSP) and Perdew-Burke-Ernzerhof (PBE) exchange correlation functions [37]. The Γ point is used for the Brillouin region sampling and the energy cutoff of the plane wave is set to 50 Ry. The equilibrium state obtained from AIMD calculations at $T = 300$ K is used as the initial state of rt-TDDFT calculations. In the rt-TDDFT simulation, an important parameter is included: TDDFT_DETAIL $= m1, m2, m\text{state}$. The default value of $m1$ is 1, and $m2$ and $m\text{state}$ are the total number of bands. We will calculate the time-dependent wave function $\psi_j(t)$, $j = 1, m\text{state}$. For the first $m1 - 1$ electronic states $\psi_j(t) = \phi_j(t)$ ($j \in [1, m1 - 1]$), meaning that these states are adiabatic eigenstate (similar to Born-Oppenheimer MD). However, for the remaining $m\text{state} - m1 + 1$ electronic states $\psi_j(t)$, they will be expanded within the adiabatic window $[m1, m2]$. The occupation numbers of $\psi_j(t)$ are held constant. They are given by the Fermi-Dirac distribution from the first self-consistent

field iteration. Therefore, the adiabatic eigenstate $\phi_i(t)$ in this algorithm extends the time-dependent wave functions $\psi_j(t)$:

$$\psi_j(t) = \phi_j(t), \quad j = 1, m1 - 1, \tag{1}$$

$$\psi_j(t) = \sum_i C_{j,i}(t)\phi_i(t), \quad j = m1, mstate, \quad i = m1, m2. \tag{2}$$

$\phi_i(t)$ stands for the eigenstates of Hamiltonian at time t,

$$H(t)\phi_i(t) \equiv \varepsilon_i(t)\phi_i(t), \tag{3}$$

$$H(t) \equiv H(t, R(t), \rho(t)), \tag{4}$$

where $R(t)$ and $\rho(t)$ represent the nuclear positions and the charge density, respectively. From Eq. (2), the evolution of wave function $\psi_j(t)$ is characterized by the coefficient $C_{i,l}(t)$:

$$\dot{C}_{j,i}(t) = -i\varepsilon_i(t)C_{j,i}(t) - \sum_l C_{j,l}(t)V_{i,l}(t), \tag{5}$$

where $V_{i,l}(t) = \langle \phi_i(t) \mid \partial\phi_l(t)/\partial t \rangle$ is the transition matrix. Due to the finite number of adiabatic states $\phi_i(t)$ determined in the expansion of Eq. (2), the procedure described above effectively reduces the original problem to a small-size matrix problem, as represented by Eq. (5). According to Eq. (3), the time-dependence of the Hamiltonian over time steps is expressed using a linearly time-dependent Hamiltonian. Specifically, within the time interval $[t_1, t_1 + \bigtriangleup t]$, the eigenstates at $t_1\{\varphi_l(t_1)\}$ are used as the basis set to expand the Hamiltonian equations. The Hamiltonian at t_1 consists only of the diagonal term $\{\varepsilon_l(t_1)\}$, while at $t_1 + \bigtriangleup t$, it is diagonal in the basis set $\{\varphi_l(t_1 + \bigtriangleup t)\}$. The Hamiltonian is assumed to evolve linearly over the interval $[t_1, t_1 + \bigtriangleup t]$. For any time t within the interval,

$$H(t) = H(t_1) + \frac{t - t_1}{\Delta t}[H(t_1 + \Delta t) - H(t_1)]. \tag{6}$$

Based on the adiabatic eigenstate basis, the linear approximation of the Hamiltonian provides a clear and well-defined characterization of the real-time time-dependent Hamiltonian $H(t)$ (with a time step $\bigtriangleup t \leqslant 0.2$ fs), which has a larger time step than the traditional real-time TDDFT (subattosecond) [35,38].

The structure, charge density, adiabatic eigenenergy, adiabatic wave function, and occupation number of eigenstates corresponding to different times are solved in the TDDFT calculation. In the DOS calculation, the total state density DOS_{total} is solved by the adiabatic wave function and adiabatic characteristic energy obtained at 100 fs or 200 fs. Additionally, density of states of occupying electrons $DOS_{occupied}$ is further obtained from the occupancy number of the eigenstate. Then, we get $DOS_{unoccupied} = DOS_{total} - DOS_{occupied}$, where the part of $DOS_{occupied}$ greater than the Fermi level is the DOS of the excited electrons, and the part of $DOS_{unoccupied}$ less than the Fermi level is the DOS of the excited holes, as shown by the occupancy of the photoexcited carrier in Fig. 3(d). In addition, the partial wave density can be calculated to project the wave function onto atomic orbitals, further obtaining the projected density of states for atoms in different orbitals [Fig. 3(e)]. In addition, a uniform A field is introduced in the reciprocal space during pulsed simulated light excitation: $H = 1/2(-i\nabla + \boldsymbol{A})^2 = 1/2(-i\nabla_x + A_x)^2 + 1/2(-i\nabla_y + A_y)^2 + 1/2(-i\nabla_z + A_z)^2$. In the pulse simulation, the external electric field of Gaussian shape used is shown in Fig. 4(a). According to the NCPP, valence electrons are represented as $Re(5d^5 6s^2)$ and $S(3s^2 3p^4)$, respectively. Thus, a $3 \times 3 \times 1$ ReS_2 supercell model with 108 atoms contains 684 valence electrons. Furthermore, under the framework of DFT wave function, the COHP is calculated using the LOBSTER package for chemical bond analysis [39,40]. The VMD package is used to further study the trajectory of rt-TDDFT-MD simulation [41].

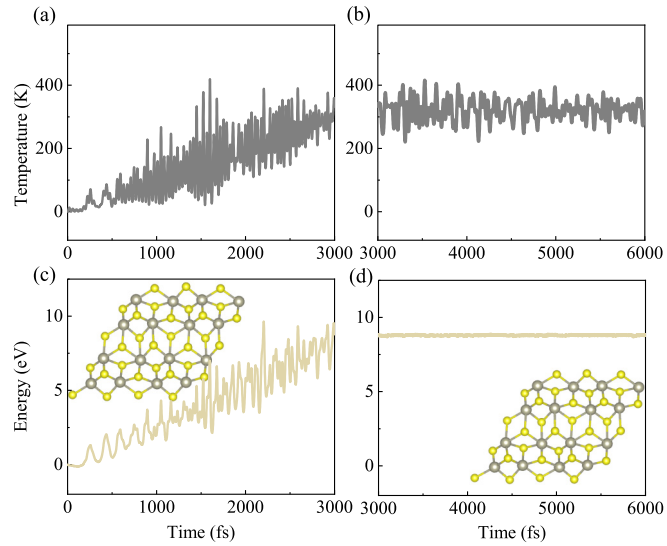

FIG. 6. [(a), (b)] Temperature and [(c), (d)] total energy curves of AIMD simulation for DS-phase ReS_2 monolayer, including heating from 1 to 300 K and hot bath at 300 K, with the initial moment as the standard. The illustrations in panels (c) and (d) show the initial structure at 1 K and the equilibrium structure at 300 K, respectively.

V. STRUCTURAL DESCRIPTION AND AIMD SIMULATIONS

We initially constructed a $3 \times 3 \times 1$ supercell of ReS_2 with 108 atoms. Following this, we performed structural relaxation and self-consistent electronic calculations to ensure an accurate representation of its electronic structure and stability. The optimized lattice constants in a and b directions are 6.38 and 6.49 Å, with an angle of 118.84° between them [42,43]. The Re-Re bond lengths of the Re_4 diamond are 2.70 and 2.81 Å. Then, to further evaluate the effect of photoexcitation on ReS_2 monolayer structure, the AIMD simulation of the ReS_2 monolayer is performed, as shown in Fig. 6. The AIMD calculations consist of two processes: heating from 1 to 300 K and a thermostatic bath at 300 K. If a constant temperature bath is applied directly, then the interactions between the system and the bath may affect the true behavior of the molecular dynamics. The heating process can assist the system in gradually reaching a more reasonable equilibrium state, helping to reduce this influence. Throughout the calculation, the distribution of electrons on energy levels in the model follows the Fermi-Dirac distribution (without electron excitation). The total energy fluctuation curve shows that the

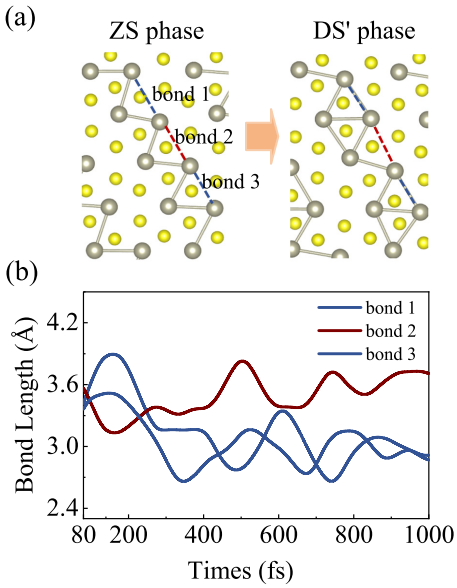

FIG. 7. (a) The atomic structures for ReS_2 monolayer in ZS phase and DS′ phase. (b) The bond-length evolution from ZS phase to DS′ phase at 4% excitation. The dark red and dark blue solid lines indicate the distance between adjacent Re atoms in the zigzag direction of the ZS phase in (a), respectively.

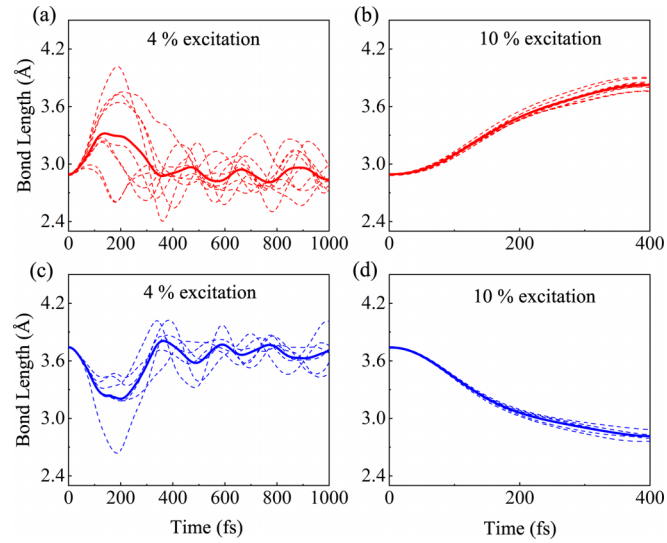

FIG. 8. The bond-length evolution under [(a), (c)] 4% and [(b), (d)] 10% electronic excitations at T = 1 K. The red and blue dashed lines represent the evolution of the $d_{\text{Re-Re}}$ bonds and $d'_{\text{Re-Re}}$ bonds. The solid lines represent the average bond length.

system is thermally stable at room temperature. Through the analysis of structural changes, it can be seen that since the average position of the atoms is not drastically deviated, all the phase structures are not distorted or deformed.

VI. PHASE TRANSITION FROM ZS TO DS′ PHASE

The ZS phase appears as an intermediate state during the transition from DS to DS′ phase. This transition is caused by the distribution of excited carriers. Specifically, a large number of photoexcited electrons fill the Re-Re antibonding state, causing an imbalance in the system. To reduce the energy of the system, the Re-Re bond breaks and recombines. The transient ZS phase is formed as the occupation of the photoexcited electrons in the conduction band broadens to cover a wider energy range. As shown in Fig. 7(a), the distances between adjacent Re atoms in the zigzag direction tend to be equal in the ZS phase at about 80 fs. The ZS phase is an unstable metastable phase that lasts only a few tens of femtoseconds. Then, the Re atoms undergo a long atomic rearrangement along the zigzag direction of the ZS phase under the action of the surrounding Re atoms. During this process, the vibration of the thermal phonons may have a significant effect, resulting in an imbalance in the structure. This imbalance causes the interaction between the atoms to change, eventually forming a new quasidiamond chain in the Re-Re zigzag direction at around 700 fs. As the thermal vibration continues, small shifts in atomic positions accumulate, prompting the system to evolve toward a more stable structural state. After 700 fs, the bond length evolution of bond 1 and bond 3 becomes consistent, while that of bond 2 evolves oppositely [Fig. 7(b)]. This timescale reflects the dynamical processes captured in real-time TDDFT simulations, and the evolution of bond lengths is consistent with the bond dissociation and recombination shown in Figs. 2(f) and 2(i).

VII. RT-TDDFT SIMULATION AT 1 K

Thermal vibration plays an absolute role in the process of temperature-induced phase transition. In the aforementioned simulations, we performed the calculation at 300 K, making it particularly crucial to account for the effects of thermal vibrations during the phase transition process. However, the sources driving structural phase transitions can be categorized into two aspects: On the one hand, the influence of thermal vibrations results in a random and disordered transition pathway; on the other hand, the transition relies on the electronic excitation process, which establishes a relatively deterministic transition pathway. To shield the action of thermal phonon, we recalculate the rt-TDDFT calculations for the lattice temperature of 1 K under 4% and 10% manual excitations (Fig. 8). It can be shown that the driving force generated by the 4% electron excitation is insufficient to induce the phase transition of ReS_2 monolayer, resulting in virtually no change in the nine Re-Re bond lengths and six non-Re-Re bond lengths within 1.0 ps. When enough valence electrons are placed at the bottom of the conduction band, a strong driving force is generated, so that the thermal phonons become less important and the atomic motion becomes more coherent, resulting in coherent dissociation and recombination of Re-Re bonds. Significantly, compared to the phase transition process at room temperature, the dissociation time of the $d_{\text{Re-Re}}$ bonds is delayed, highlighting the critical role of thermal phonon vibrations at room temperature. At room temperature, the presence of thermal phonon effectively reduces the excited electrons required to drive the phase transition.

ACKNOWLEDGMENTS

This work was financially supported by the National Natural Science Foundation of China (Grants No. 62375086, No. 62274066, and No. 62090013), the Projects of Science and Technology Commission of Shanghai Municipality (Grant No. 21JC1402100), and the Program for Professor of Special Appointment (Eastern Scholar) at Shanghai Institutions of Higher Learning.

DATA AVAILABILITY

The data that support the findings of this study are available from the corresponding author upon reasonable request.

[1] W. Zhai, Z. Li, Y. Wang, L. Zhai, Y. Yao, S. Li, L. Wang, H. Yang, B. Chi, J. Liang, Z. Shi, Y. Ge, Z. Lai, Q. Yun, A. Zhang, Z. Wu, Q. He, B. Chen, Z. Huang, and H. Zhang, Phase engineering of nanomaterials: Transition metal dichalcogenides, Chem. Rev. **124**, 4479 (2024).

[2] S. Park, C. Kim, S. O. Park, N. K. Oh, U. Kim, J. Lee, J. Seo, Y. Yang, H. Y. Lim, S. K. Kwak, G. Kim, and H. Park, Phase engineering of transition metal dichalcogenides with unprecedentedly high phase purity, stability, and scalability via molten-metal-assisted intercalation, Adv. Mater. **32**, 2001889 (2020).

[3] L. Y. Chen, L. Chen, H. L. Chen, K. Jiang, L. Q. Zhu, L. Y. Shang, Y. W. Li, S. J. Gong, and Z. G. Hu, Phase transition in $WSe_{2-x}Te_x$ monolayers driven by charge injection and pressure: A first-principles study, Nanoscale **16**, 6618 (2024).

[4] M. Rahman, K. Davey, and S. Qiao, Advent of 2D rhenium disulfide (ReS_2): Fundamentals to applications, Adv. Funct. Mater. **27**, 1606129 (2017).

[5] S. Tongay, H. Sahin, C. Ko, A. Luce, W. Fan, K. Liu, J. Zhou, Y. S. Huang, C. H. Ho, J. Yan, D. F. Ogletree, S. Aloni, J. Ji, S. Li, J. Li, F. M. Peeters, and J. Wu, Monolayer behaviour in bulk ReS_2 due to electronic and vibrational decoupling, Nat. Commun. **5**, 3252 (2014).

[6] T. Wen, M. Zhang, J. Li, C. Jiao, S. Pei, Z. Wang, and J. Xia, Orientation-polarization dependence of pressure-induced Raman anomalies in anisotropic 2D ReS_2, Nanoscale Horiz. **8**, 516 (2023).

[7] X. Li, X. Dai, D. Tang, X. Wang, J. Hong, C. Chen, Y. Yang, J. Lu, J. Zhu, Z. Lei, K. Suenaga, F. Ding, and H. Xu, Realizing the intrinsic anisotropic growth of 1T′ ReS_2 on selected Au(101) substrate toward large-scale single crystal fabrication, Adv. Funct. Mater. **31**, 2102138 (2021).

[8] D. Liu, J. Hong, X. Li, X. Zhou, B. Jin, Q. Cui, J. Chen, Q. Feng, C. Xu, T. Zhai, K. Suenaga, and H. Xu, Synthesis of 2H-1T′ WS_2-ReS_2 heterophase structures with atomically sharp interface via hydrogen-triggered one-pot growth, Adv. Funct. Mater. **30**, 1910169 (2020).

[9] F. Cui, C. Wang, X. Li, G. Wang, K. Liu, Z. Yang, Q. Feng, X. Liang, Z. Zhang, S. Liu, Z. Lei, Z. Liu, H. Xu, and J. Zhang, Tellurium-assisted epitaxial growth of large-area, highly crystalline ReS_2 atomic layers on mica substrate, Adv. Mater. **28**, 5019 (2016).

[10] P. Aggarwal, H. Sheoran, P. Bisht, O. K. Prasad, C.-H. Chung, E. Y. Chang, B. R. Mehta, and R. Singh, Synthesis of a large area ReS_2 thin film by CVD for in-depth investigation of resistive switching: Effects of metal electrodes, channel width and noise behaviour, Nanoscale **15**, 14109 (2023).

[11] D. Zhou, Y. Zhou, C. Pu, X. Chen, P. Lu, X. Wang, C. An, Y. Zhou, F. Miao, C.-H. Ho, J. Sun, Z. Yang, and D. Xing, Pressure-induced metallization and superconducting phase in ReS_2, npj Quant. Mater. **2**, 19 (2017).

[12] B. Küçüköz, B. Munkhbat, and T. O. Shegai, Boosting second-harmonic generation in monolayer rhenium disulfide by reversible laser patterning, ACS Photonics **9**, 518 (2022).

[13] F. Zheng, D. Guo, L. Huang, L. W. Wong, X. Chen, C. Wang, Y. Cai, N. Wang, C.-S. Lee, S. P. Lau, T. H. Ly, W. Ji, and J. Zhao, Sub-nanometer electron beam phase patterning in 2D materials, Adv. Sci. **9**, 2200702 (2022).

[14] Y. C. Lin, H. P. Komsa, C. H. Yeh, T. Bjorkman, Z. Y. Liang, C. H. Ho, Y. S. Huang, P. W. Chiu, A. V. Krasheninnikov, and K. Suenaga, Single-layer ReS_2: Two-dimensional semiconductor with tunable in-plane anisotropy, ACS Nano **9**, 11249 (2015).

[15] W. Yu, Z. Wang, Z. X. Zhao, J. Wang, T. S. Herng, T. Ma, Z. Zhu, J. Ding, G. Eda, S. J. Pennycook, Y. P. Feng, and K. P. Loh, Domain engineering in ReS_2 by coupling strain during electrochemical exfoliation, Adv. Funct. Mater. **30**, 2003057 (2020).

[16] G. Ghimire, K. P. Dhakal, W. Choi, Y. A. Esthete, S. J. Kim, T. T. Tran, H. Lee, H. Yang, D. L. Duong, Y. M. Kim, and J. Kim, Doping-mediated lattice engineering of monolayer ReS_2 for modulating in-plane anisotropy of optical and transport properties, ACS Nano **15**, 13770 (2021).

[17] H. W. Liu, W. H. Liu, Z. J. Suo, Z. Wang, J. W. Luo, S. S. Li, and L. W. Wang, Unifying the order and disorder dynamics in photoexcited VO_2, Proc. Natl. Acad. Sci. USA **119**, e2122534119 (2022).

[18] W. H. Liu, J. W. Luo, S. S. Li, and L. W. Wang, Microscopic force driving the photoinduced ultrafast phase transition: Time-dependent density functional theory simulations of $IrTe_2$, Phys. Rev. B **102**, 184308 (2020).

[19] X. P. Liu, D. Legut, and Q. F. Zhang, Photoinduced ultrafast phase transition in bilayer CrI_3, J. Phys. Chem. Lett. **14**, 7744 (2023).

[20] W.-H. Liu, J.-W. Luo, S.-S. Li, and L.-W. Wang, Dynamic short-range correlation in photoinduced disorder phase transitions, Phys. Rev. B **105**, 224306 (2022).

[21] L. Chen, L. Chen, H. Chen, Y. Li, L. Shang, L. Zhu, J. Zhang, S. Gong, and Z. Hu, Role of microscopic coherent force and hot-carrier cooling in photoinduced phase transition for chalcogenide phase-change materials, Phys. Rev. B **110**, 144105 (2024).

[22] L. Bassman, A. Krishnamoorthy, H. Kumazoe, M. Misawa, F. Shimojo, R. K. Kalia, A. Nakano, and P. Vashishta, Electronic origin of optically-induced sub-picosecond lattice dynamics in $MoSe_2$ monolayer, Nano Lett. **18**, 4653 (2018).

[23] B. Peng, H. Zhang, W. Chen, B. Hou, Z.-J. Qiu, H. Shao, H. Zhu, B. Monserrat, D. Fu, H. Weng, and C. M. Soukoulis,

Sub-picosecond photo-induced displacive phase transition in two-dimensional $MoTe_2$, npj 2D Mater. Appl. **4**, 14 (2020).

[24] L. Chen, A. Y. Cui, M. Li, S. B. Li, S. J. Gong, K. Jiang, J. Z. Zhang, L. Q. Zhu, L. Y. Shang, Y. W. Li, Z. G. Hu, and J. H. Chu, Optical excitation-induced ultrafast amorphization in the Y-Sb-Te alloy system: Insights from real-time time-dependent DFT with molecular dynamics calculations, Phys. Rev. B **106**, 214110 (2022).

[25] B. Peng, G. F. Lange, D. Bennett, K. Wang, R.-J. Slager, and B. Monserrat, Photoinduced electronic and spin topological phase transitions in monolayer bismuth, Phys. Rev. Lett. **132**, 116601 (2024).

[26] K. Wu, B. Chen, S. Yang, G. Wang, W. Kong, H. Cai, T. Aoki, E. Soignard, X. Marie, A. Yano, A. Suslu, B. Urbaszek, and S. Tongay, Domain architectures and grain boundaries in chemical vapor deposited highly anisotropic ReS_2 monolayer films, Nano Lett. **16**, 5888 (2016).

[27] C. H. Ho, Y. S. Huang, J. L. Chen, T. E. Dann, and K. K. Tiong, Electronic structure of ReS_2 and $ReSe_2$ from first-principles calculations, photoelectron spectroscopy, and electrolyte electroreflectance, Phys. Rev. B **60**, 15766 (1999).

[28] M. Kertesz, and R. Hoffmann, Octahedral vs. trigonal-prismatic coordination and clustering in transition-metal dichalcogenides, J. Am. Chem. Soc. **106**, 3453 (1984).

[29] M. Bernardi, D. Vigil-Fowler, J. Lischner, J. B. Neaton, and S. G. Louie, Ab initio study of hot carriers in the first picosecond after sunlight absorption in silicon, Phys. Rev. Lett. **112**, 257402 (2014).

[30] W. W. Meng, X. M. Wang, Z. W. Xiao, J. B. Wang, D. B. Mitzi, and Y. F. Yan, Parity-forbidden transitions and their impact on the optical absorption properties of lead-free metal halide perovskites and double perovskites, J. Phys. Chem. Lett. **8**, 2999 (2017).

[31] X. Chen, B. Lei, Y. Zhu, J. Zhou, M. Gao, Z. Liu, W. Ji, and W. Zhou, Diverse spin-polarized in-gap states at grain boundaries of rhenium dichalcogenides induced by unsaturated Re-Re bonding, ACS Mater. Lett. **3**, 1513 (2021).

[32] L. Chen, L. Wang, K. Jiang, J. Z. Zhang, Y. W. Li, L. Y. Shang, L. Q. Zhu, S. J. Gong, and Z. G. Hu, Optically induced multistage phase transition in coherent phonon-dominated α-GeTe, J. Phys. Chem. Lett. **14**, 5760 (2023).

[33] M.-X. Guan, X.-B. Liu, D.-Q. Chen, X.-Y. Li, Y.-P. Qi, Q. Yang, P.-W. You, and S. Meng, Optical control of multistage phase transition via phonon coupling in $MoTe_2$, Phys. Rev. Lett. **128**, 015702 (2022).

[34] W. H. Liu, J. W. Luo, S. S. Li, and L. W. Wang, The seeds and homogeneous nucleation of photoinduced nonthermal melting in semiconductors due to self-amplified local dynamic instability, Sci. Adv. **8**, eabn4430 (2022).

[35] Z. Wang, S. S. Li, and L. W. Wang, Efficient real-time time-dependent density functional theory method and its application to a collision of an ion with a 2D material, Phys. Rev. Lett. **114**, 063004 (2015).

[36] W. L. Jia, Z. Y. Cao, L. Wang, J. Y. Fu, X. B. Chi, W. G. Gao, and L. W. Wang, The analysis of a plane wave pseudopotential density functional theory code on a GPU machine, Comput. Phys. Commun. **184**, 9 (2013).

[37] D. R. Hamann, Optimized norm-conserving Vanderbilt pseudopotentials, Phys. Rev. B **88**, 085117 (2013).

[38] J. Ren, N. Vukmirovic, and L. W. Wang, Nonadiabatic molecular dynamics simulation for carrier transport in a pentathiophene butyric acid monolayer, Phys. Rev. B **87**, 205117 (2013).

[39] S. Maintz, V. L. Deringer, A. L. Tchougreeff, and R. Dronskowski, Analytic projection from plane-wave and PAW wavefunctions and application to chemical-bonding analysis in solids, J. Comput. Chem. **34**, 2557 (2013).

[40] S. Maintz, V. L. Deringer, A. L. Tchougreeff, and R. Dronskowski, LOBSTER: A tool to extract chemical bonding from plane-wave based DFT, J. Comput. Chem. **37**, 1030 (2016).

[41] W. Humphrey, A. Dalke, and K. Schulten, VMD: Visual molecular dynamics, J. Mol. Graphics **14**, 33 (1996).

[42] Z. Sun, H. Lv, Z. Zhuo, A. Jalil, W. Zhang, X. Wu, and J. Yang, A new phase of the two-dimensional ReS_2 sheet with tunable magnetism, J. Mater. Chem. C **6**, 1248 (2018).

[43] Y. D. Cao, Y. H. Sun, S. F. Shi, and R. M. Wang, Anisotropy of two-dimensional ReS_2 and advances in its device application, Rare Met. **40**, 3357 (2021).